Cyclic oxidation behaviour of N-type (Zr,Ti)Ni(Sn,Sb) and P-type (Zr,Ti)Co(Sn,Sb) thermoelectric materials

Gurtaran, Mikdat; Zhang, Zhenxue; Li, Xiaoying; Dong, Hanshan

DOI:
10.1016/j.jmrt.2024.05.136

Document Version
Publisher's PDF, also known as Version of record

Citation for published version (Harvard):
Gurtaran, M, Zhang, Z, Li, X & Dong, H 2024, 'Cyclic oxidation behaviour of N-type (Zr,Ti)Ni(Sn,Sb) and P-type (Zr,Ti)Co(Sn,Sb) thermoelectric materials', *Journal of Materials Research and Technology*, vol. 30, pp. 7476-7484. https://doi.org/10.1016/j.jmrt.2024.05.136

Journal of Materials Research and Technology 30 (2024) 7476–7484

Contents lists available at ScienceDirect

Journal of Materials Research and Technology

journal homepage: www.elsevier.com/locate/jmrt

Cyclic oxidation behaviour of N-type (Zr,Ti)Ni(Sn,Sb) and P-type (Zr,Ti)Co(Sn,Sb) thermoelectric materials

Mikdat Gurtaran *, Zhenxue Zhang, Xiaoying Li, Hanshan Dong

School of Metallurgy and Materials, The University of Birmingham, Birmingham, B15 2TT, UK

ARTICLE INFO

Keywords:
Thermoelectric materials
Half-heusler
Cyclic oxidation
Diffusion

ABSTRACT

In this study, the fabricated Hf-free N-type (Zr,Ti)Ni(Sn,Sb) and P-type (Zr,Ti)Co(Sn,Sb) thermoelectric materials were subjected to cyclic oxidation testing at 500 °C for 10, 30, and 50 cycles. The oxidation behaviour of the materials was systematically investigated by evaluating mass gain to study the oxidation kinetics and by analysing surface morphology, phase constitution and elemental distribution to investigate the oxidation mechanism. The results indicated that both of the materials were severely oxidised during the cyclic oxidation testing, and the mass gain followed the parabolic kinetics and the parabolic rate constant (k_p) being 0.006165 $mg^2cm^{-4}s^{-1}$ and 0.000109 $mg^2cm^{-4}s^{-1}$ for the N-type and the P-type TE materials, respectively. Alternated multilayers of Ni_3Sn_4+SnO_2+$(Zr,Ti)O_2$ and CoSb + SnO_2+Sb_2O_4+$(Zr,Ti)O_2$ were identified on the surface of the N-type and P-type materials, respectively, after the cyclic testing, which would deteriorate the thermoelectric performance of the materials. The outcome of this study strongly suggests that it is essential to improve the oxidation resistance and the thermal stability of the N-type (Zr,Ti)Ni(Sn,Sb) and P-type (Zr,Ti)Co(Sn,Sb) thermoelectric materials for high-temperature applications.

1. Introduction

Thermoelectric materials (TE) are crucial for efficiently converting waste heat into electrical energy to meet the ever-growing energy demands [1,2] and the net-zero target, which has attracted extensive research interests in developing new TE materials with a high figure of merit, zT value ($zT = S^2\sigma\kappa^{-1}T$) for high thermoelectric performance, combining the Seebeck coefficient (S), electrical conductivity (σ), thermal conductivity (κ), and absolute temperature (T) [3,4]. Many thermoelectric materials are being explored for power generation applications, such as GeTe [5], Bi_2Te_3 [6], PbTe [7,8], and half-Heusler compounds [9]. Researchers have been also working on improving the zT value of such commercially available thermoelectric materials as Bi-Te [10–12] and Pb–Te [13–15] compounds. However, these TE materials contain critical raw element Bi and toxic heavy metal Pb. Therefore, the state-of-the-art half-Heusler [16–18], SnTe [19–21], and MgSi-based [22–24] TE materials, with comparable or superior thermoelectric performance and lower ecological impact, are being rapidly developed.

As most half-Heusler materials contain Hafnium (Hf), a costly critical raw element, researchers have recently developed more cost-effective and sustainable Hf-free and Hf-substituted half-Heusler materials [25,26]. It is known that the oxidation behaviour of TE materials is highly composition dependent. Removal of chemically active element Hf from Hf-containing half-Heusler alloys would change their oxidation behaviour. Notably, Hf-free half-Heusler thermoelectric materials have gained recognition for their remarkable thermoelectric performance because of the high zT values between 0.7 and 1.5 as a function of the working temperature, indicating efficient heat-to-electricity conversion [27,28]. Chauhan et al. [16] increased the zT value of Hf-free half-Heusler materials to approximately 0.8 at 500 °C. Zhang et al. [29] produced Hf-free N-type ZrNiSn with a zT value of 0.78 at 500 °C. Min et al. [30] achieved a significantly improved zT value of 0.89 for Nb-doped ZrNiSn half-Heusler compounds. Further progress was made by Nguyen et al. [17], producing Hf-free N-type $(Ti_{0.5}Zr_{0.5})_{1-x}Nb_xNiSn$ half-Heusler material via a fast production technique, which is a combination of arc-melting, melt spinning and spark plasma sintering. They obtained a zT value of 1.19 at 600 °C with the optimised composition with x = 0.0125.

However, thermal stability and oxidation behaviour at high service temperatures are concerns for thermoelectric generators. In particular, most TE generators and devices work in frequent heating and cooling

* Corresponding author.
E-mail address: m.gurtaran@bham.ac.uk (M. Gurtaran).

https://doi.org/10.1016/j.jmrt.2024.05.136
Received 5 April 2024; Received in revised form 9 May 2024; Accepted 15 May 2024
Available online 16 May 2024

thermal cycles, which present an even more challenging environment [31]. Kang et al. reported that the power output of thermoelectric generators involving MCoSb (P-type) materials was reduced by 50% after 120 h at 823 K in air [32]. To ensure sufficient thermal stability, thermoelectric materials must have high oxidation resistance [33,34] to prevent surface damage, segregation and sublimation [35,36]. This is because such oxidation-related surface damages can act as barriers to the movement of charged particles and heat carriers, thus reducing electrical conductivity and hence the performance of TE materials. For example, it is reported by Kikuchi et al. that the electrical resistivity of polycrystalline $Ba_8Ga_xAl_ySi_{46-x-y}$ type-I clathrates was increased with increasing temperature, leading to a significant decrease in the zT value [37]. Additionally, sublimation of elements such as Sn and Sb at high temperatures alters the composition and critical properties of TE materials, possibly negatively impacting electrical and thermal conductivity. Therefore, understanding the oxidation and sublimation behaviour and the mechanisms involved is vital to designing and developing high-performance and long-life thermoelectric materials as well as providing essential information for developing advanced surface coatings to protect TE materials from oxidation and sublimation.

The present study is focused on investigating the oxidation behaviour of a new generation of Hf-free and cost-effective N-type (Zr,Ti)Ni(Sn,Sb) and P-type (Zr,Ti)Co(Sn,Sb) thermoelectric materials produced by mechanical alloying followed by spark plasma sintering. The fabricated TE blocks were subjected to cyclic oxidation testing between 500 °C and room temperature for 10, 30 and 50 cycles in air since the majority of TE materials experience continuous heating and cooling cycles in practical applications. The oxidation behaviour and mechanisms of the N and P-type samples were investigated by mass gain measurements, surface morphology evolution, cross-section layer characterisation and phase transition analyses. Future research directions for developing thermoelectric materials with improved thermal stability and advanced oxidation protection surface coatings are proposed based on the new insights into the oxidation behaviours and mechanism of the Hf-free half-Heusler TE materials.

2. Experimental

2.1. Fabrication of TE materials

The test samples (with dimensions of approximately 4 × 0.5 × 0.5 cm^3) were produced by MATRES Scrl (Italy) and the chemical composition is shown in Table 1. To achieve the desired concentration of materials, industrial metal powders (Zr, Ti, Ni, Co, Sn, and Sb) were obtained, and the mechanical alloying was conducted in an inert environment using the high-energy ball mill technique, which allowed for controlled impact velocities as well as minimising defects observed in traditional alloying methods. The green compact of the metal powders was sintered for 4 min at 800 °C and under a pressure of 500 kg/cm^2 using a uniaxial press (DSP 475, Dr. Fritsch).

2.2. Cyclic oxidation testing

The testing samples were cut to dimensions of 0.5 × 0.5 × 0.5 cm^3 and ground up to 1200 grit using SiC abrasive papers. The samples were then ultrasonically cleaned in acetone for 5 min. Cyclic oxidation testing was conducted in a muffle furnace, and each test sample was individually placed in a ceramic container. When the temperature reached 500 °C, the samples with ceramic containers were swiftly loaded into the furnace to avoid a sharp temperature drop. It only took about 2 min to reach the set temperature of 500 °C, and the samples remained at 500 °C for 1 h before they were removed from the furnace and cooled in air to room temperature. This designed thermal cycle (Fig. 1) was repeated 10, 30, and 50 times for all N and P-type samples. Before and after each test cycle, the weight of the samples within the ceramic container was measured using a high-precision scale (Ohaus, Switzerland) with an accuracy of 10^{-4} g. Three repeated measurements were made, and the average was reported. Detailed sample codes and their corresponding conditions are summarised in Table 2.

Table 1
Chemical composition (at. %) of the fabricated thermoelectric materials.

Materials	Code	Elements					
		Ti	Ni	Co	Zr	Sn	Sb
(Zr,Ti)Ni(Sn,Sb)	N	17.1	33.5	0	16.3	32.3	<1.0
(Zr,Ti)Co(Sn,Sb)	P	16.4	0	29.1	18.1	10.7	25.7

2.3. Microstructural characterisation

Comprehensive microstructure analysis was carried out on N and P samples before and after cyclic oxidation tests. Surface and cross-sectional microstructures of the TE materials were investigated by scanning electron microscopy using Jeol 7000 and Apreo2 SEM (Jeol-UK Ltd., UK and Thermofisher Scientific, UK, respectively) with an EDX device for analysing chemical concentration and distribution. Samples were XRD scanned by a Proto AXRD diffractometer employing a Cu-Kα source (λ = 1.540598 Å), and phase identification was carried out using High Score Plus software.

3. Results

3.1. Mass gain of cyclic-oxidation tested N & P-type TE samples

The mass gains of the tested samples were measured and calculated after each cycle, and the obtained data are presented in Fig. 2a. For as-produced N and P-type samples, the mass gain shows a parabolic trend. This is confirmed by the straight lines shown in Fig. 2b when plotting the square of the mass gain $(\Delta m/A)^2$ against the number of cycles (N), which is proportional to the time (t). The mass gain of the N-type samples increased much faster than that of the P-type samples throughout the cyclic oxidation testing process. At the end of 50 cycles, the final mass gain for the N-type sample was 5.8 mg/cm^2, while it was only 2.1 mg/cm^2 for the P-type sample.

3.2. Phase changes after cyclic oxidation tests

XRD patterns of as-received N and P-type samples are compared to the oxidised samples as shown in Fig. 3. Before oxidation, the diffraction pattern of the N-type sample shows a single half-Heusler phase of (Zr,Ti)Ni(Sn,Sb) (cubic, a = 0.603 nm, PDF: 01-089-7155), crystalising in the

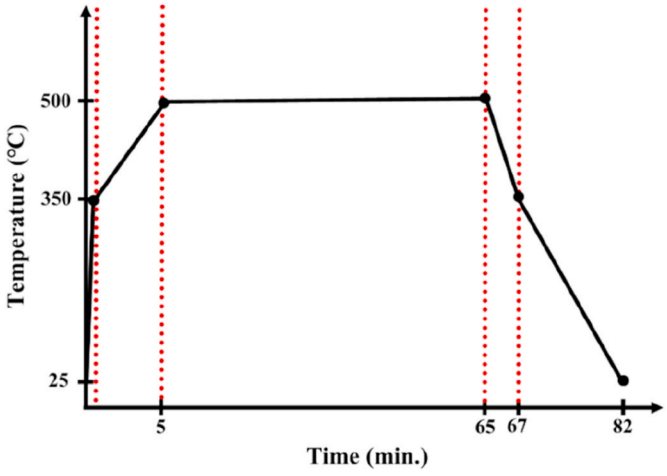

Fig. 1. Schematic representation of one thermal cycle of the oxidation testing.

Table 2
Sample codes and corresponding processing details.

Sample Code		Oxidation cycles at 500 °C
N	P	0 cycle (As-produced N-type and P-type pellets)
N-10	P-10	10 cycles
N-30	P-30	30 cycles
N-50	P-50	50 cycles

C1b structure type. The main phase formed in the P-type material is a typical half-Heusler phase of (Zr,Ti)Co(Sn,Sb) with the crystal structure of C1b, a = 0.599 nm. Some traces of weak peaks can be tentatively indexed to Sb (rhombohedral, a = b = 0.43 nm, c = 1.12 nm, PDF: 01-085-1324).

After cyclic oxidation tests, substantial alterations of phase constituents on the surface of N-type and P-type materials were observed. As for N-type samples, crystallographic reflections corresponding to SnO_2 (tetragonal, a = b = 0.473 nm, c = 0.318 nm, PDF: 01-070-4177), Ni_3Sn_4, (monoclinic, a = 1.22 nm, b = 0.405 nm, c = 0.521 nm, PDF: 03-065-4310) and $(Zr,Ti)O_2$ (orthorhombic, a = 0.504 nm, b = 0.509 nm, c = 0.525 nm, PDF: 00-037-1413) phases were identified for all cyclic tested samples. However, the intensity of the diffraction peaks of SnO_2 and Ni_3Sn_4 phases exhibited high intensity when the number of oxidation cycles increased. Meanwhile, the $(Zr,Ti)O_2$ phase shows low intensity for all cyclic oxidation tested samples.

The XRD patterns of P-type material after cyclic oxidation tests are presented in Fig. 3b. For all cyclic oxidation tested samples, four phases can be identified corresponding to SnO_2 (tetragonal, a = b = 0.473 nm, c = 0.318 nm, PDF: 01-077-0447), SbCo (hexagonal, a = b = 0.39 nm, c = 0.517 nm, PDF: 96-154-1040), $(Zr,Ti)O_2$ (monoclinic, a = 0.507, b = 0.521 nm, c = 0.519 nm, PDF: 96-210-8456), and Sb_2O_4 (orthorhombic, a = 0.543 nm, b = 0.481 nm, c = 1.176 nm, PDF: 01-071-0564), which are markedly different from the original phase composition of P-type material. Notably, the diffraction peaks attributed to SbCo and SnO_2 exhibited relatively strong intensities, while reflections corresponding to the $(Zr,Ti)O_2$ phase were very weak for the P-50 sample (Fig. 3b).

3.3. Effect of cyclic testing on surface morphology

Backscattering electron images (BEI) of N and P samples, and SEM images of N-10, N-50, P-10 and P-50 samples are given in Fig. 4. The surfaces of the N and P samples (Fig. 4a&d) are greyish with a few light and dark small patches. EDX chemical composition analysis in the dark regions (Fig. 4a) of the N sample identifies 16.3% Ti, 28.8% Ni, 21.7% Zr, 33.1% Sn and 0.1% Sb (see Table 3). In the light regions (Fig. 4a), EDX analysis revealed a high concentration of Ni (40.1 at.%) and Sn (50.4 at.%) (Table 3). Upon comparing the chemical composition of the dark and bright patches in the N sample (Table 1), it can be seen that high Zr and Ti contents led to the change of colour from light grey to dark grey, while regions rich in Ni and Sn appeared bright. A similar feature was observed in the P-type sample (Fig. 4d) where Zr-rich regions are in dark grey contrast, while the white contrasted patches are rich in Co and Sb (Table 3).

After 10 cycles of oxidation, some cauliflower-like patterns were observed on the surface of the N sample without noticeable delamination features (Fig. 4b). When the oxidation cycles increased, both large areas with fine particles and jigsaw-like patches were observed, and a typical surface morphology of the N-50 sample is shown in Fig. 4c. EDX surface composition analysis revealed enrichment of Sn, Ni and O from the area with fine particles and high content of Zr, Ti and O from the jigsaw-like patches, as denoted in Fig. 4c. Limited delamination of the oxides was observed from the surface of the N-50 sample.

Multiple microparticles rich in elements of Co, Sn and Sb and small cracks/delamination were observed on the cyclic oxidation-tested P-type samples (Fig. 4e&f). When increasing the cycles of the oxidation testing, the particles on the surface and the cracks and delamination of the surface oxide layer increased as shown in Fig. 4e&f for P-10 and P-50 samples respectively.

3.4. Cross-sectional layer structure after cyclic oxidation testing

The cross-sectional layer structures of cyclic-oxidation tested N-type and P-type samples were observed under backscattering electron image mode (Fig. 5). A multilayered structure was formed on all cyclic oxidation tested samples with the thickness of the multilayers and the cracks increased with the number of cycles. It can be seen that the individual layers within the multilayers showed distinct grey and white contrasts, indicating element segregation and selective oxidation during the cyclic oxidation testing of the material. For the N-10 sample, the multilayer structure consists of thick repeated layers on the top surface as well as thinner alternated layers below the thick layers, as can be seen in Fig. 5a. The thickness of the multilayered oxide structure of the N-10 sample is greater than that of the P-10 sample (Fig. 5a&b), which means that the N-type material is oxidised faster than the P-type, leading to more increase in the mass gain (see Fig. 2). Significant structural defects were observed, the extent of which increased with the oxidation cycles. Severe large cracks were observed near the interface between the matrix and the surface layer for the N-50 sample (Fig. 5c), while for the P-50 sample, the cracks developed along the interfaces between multilayers (Fig. 5d). As evidenced from the surface of the oxide structure, deep surface oxide spallation occurred especially for the N-50 sample (Fig. 4e), which reduced the thickness of the remained oxide layer observed on the cross section. Significant structural defects were observed, the extent of which increased with the oxidation cycles. Severe large cracks were observed near the interface between the matrix and the surface layer for the N-50 sample (Fig. 5c), while for the P-50 sample, the cracks developed along the interfaces between multilayers (Fig. 5d).

The cross-sectional EDS line-scan analysis (Fig. 6) across the multilayered structure provides element distribution through each thin layer

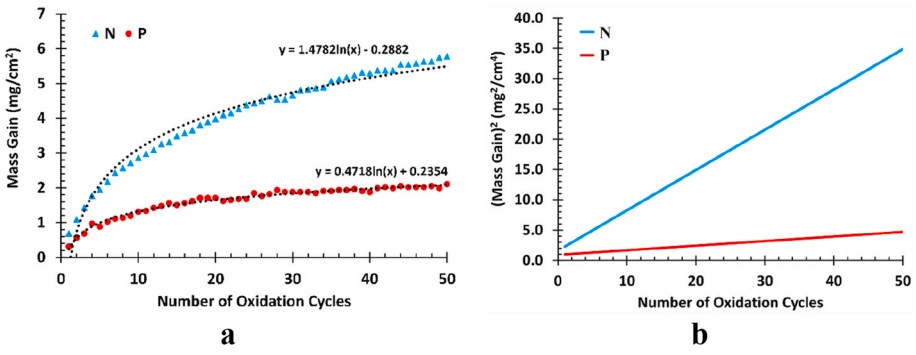

Fig. 2. Mass gain (a) and the square of the mass gain (b) of the oxidised N and P-type samples as a function of the number of cycles.

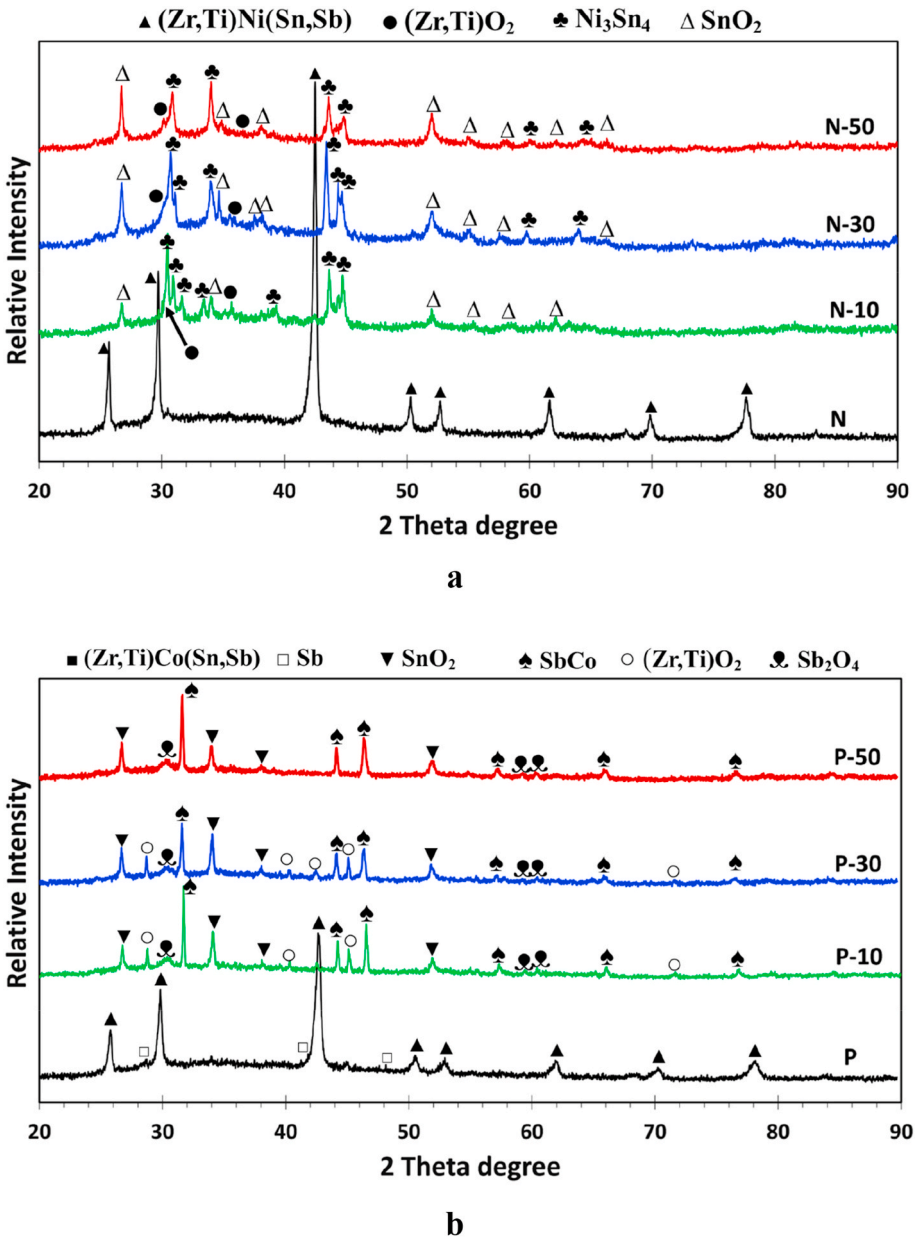

Fig. 3. XRD patterns of (a) N-10, N-30 and N-50 samples compared with the N sample, (b) P-10, P-30 and P-50 samples compared with the P sample.

for N-10 and P-10 samples. It is observed that Zr, Ti together with oxygen exhibit prominently heightened signals in the grey layers of the N-10 sample (dashed line in Fig. 6a), whereas Ni, Sn, and Sb show high intensity in the white layers (solid line in Fig. 6a). For the P-10 sample, Zr, Ti and oxygen have high concentrations in the grey layer (dashed line in Fig. 6b), and Co and Sb display high intensity in the white layers (solid line in Fig. 6b). However, Sn content shows a small fluctuation within grey and white layers for the P-10 sample, indicating moderate segregation of the element during the cyclic oxidation.

4. Discussion

4.1. Cyclic oxidation of N-type material

SEM images in Fig. 4a&d shows the overall single-phase contrast of the matrix for both as-received N-type and P-type materials although small patches of element segregation are presented (Table 3). XRD pattern analysis confirmed the Hf-free half-Heusler single phase of (Zr, Ti)Ni(Sn,Sb) for the N-type and (Zr,Ti)Co(Sn,Sb) for the P-type materials. As can be seen from Fig. 4, the surface morphology of the samples changed completely after the cyclic oxidation tests with different features for the N-type and P-type materials. The surface of the N sample presents cauliflower-like oxide features after 10 cycles of oxidation tests. EDX analysis revealed a high content of Sn in these areas, indicating that these cauliflower-like oxides were initiated from the original Sn(Ni) rich areas, as denoted in Fig. 4a, where oxygen reacted with Sn to form SnO_2. After long cycle oxidation, the cauliflower-like SnO_2 oxide areas merged into flat large patches decorated with nano-particles; the other surface areas formed jigsaw-like $(Zr,Ti)O_2$ (Fig. 4c), which were initiated from the original (Zr,Ti)-rich particles, as denoted in Fig. 4a. SEM images (Fig. 5a&c) and EDX line scan analysis (Fig. 6a) reveal that the contents of the elements (Zr, Ti, Ni, Sn, Sb and O) fluctuate periodically along the oxide case corresponding to the multilayered structure. The XRD results (Fig. 3a) confirmed the oxidation products of $(Zr,Ti)O_2$, SnO_2 and Ni_3Sn_4 compounds. This indicates that the cyclic oxidation between room temperature and 500 °C has led to the formation of alternately repeated

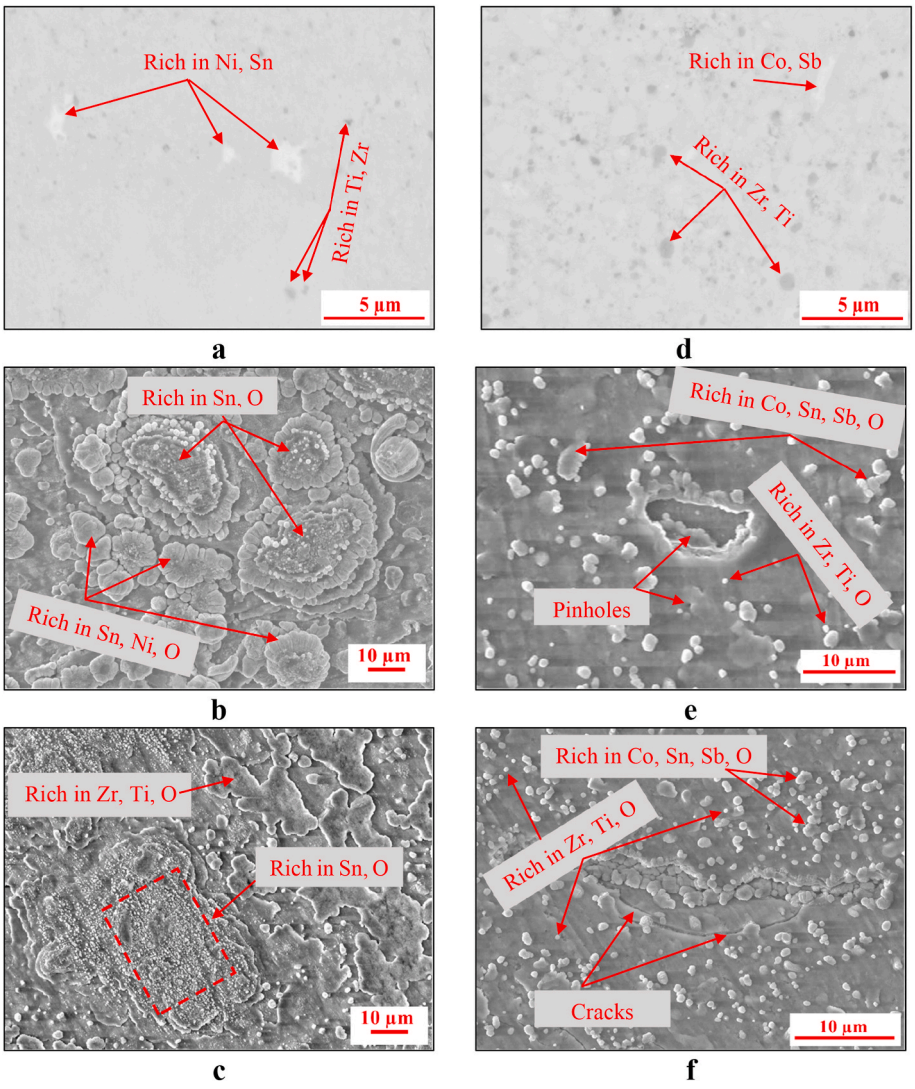

Fig. 4. Backscattered electron images of the (a) as-produced N compared with SEM images of (b) N-10 and (c) N-50; and (d) as-produced P samples compared with SEM images of (e) P-10 and (f) P-50.

Table 3
EDS analyses (at. %) of the dark and bright points on the surface of the as-received N and P samples.

Samples		Ti	Ni	Co	Zr	Sn	Sb
N	Bright Point	4.3	40.1	–	4.4	50.4	–
	Dark Point	16.3	28.8	–	21.7	33.1	0.1
P	Bright Point	10.1	–	29.3	24.7	4.9	31.0
	Dark Point	11.2	–	18.4	44.8	4.2	21.3

layers of oxides ($(Zr,Ti)O_2 + SnO_2$) and Ni_3Sn_4.

Formation of this alternated multilayer structure can be considered as a competitive process between internal oxidation and external oxidation as schematically illustrated in Fig. 7. At the beginning of oxidation, oxygen diffused inward into the surface of the TE material. Those small areas with high concentrations of Sn, (Zr,Ti) reacted with oxygen to form SnO_2 and $(Zr,Ti)O_2$ (Fig. 7b&c) featured as cauliflower-like and jigsaw-shaped patches, respectively (Fig. 4a&b). In the meantime, oxygen further diffused into the subsurface of (Zr,Ti)Ni(Sn,Sb), where those elements with low enthalpies of formation oxides, such as Zr, Ti and Sn (Fig. 8 [38,39]) would form $(Zr,Ti)O_2$ and SnO_2. While those unoxidised Ni and Sn remain in-situ forming Ni_3Sn_4, and the residual Sn diffused to the outside surface driven by the reduced surface energy [40] where Sn is oxidised to form SnO_2 (Fig. 7c). Detailed information on the oxidation of half-Heusler NiTiSn multi-phased material with the formation of the Ni_3Sn_4 and oxide phases determined by the calculated ternary phase diagram can be found in Ref. [41].

Following that, the low enthalpy oxide forming elements, such as Zr, Ti and Sn diffused outward to the interface between the formed oxide layer and the matrix to form $(Zr,Ti)O_2$ and SnO_2, as schematically shown in Fig. 7d, while unmigrated Ni and part of Sn elements formed additional layer of Ni_3Sn_4 intermetallic compound beneath the oxide layer with the remaining Sn diffusing to the top of the Ni_3Sn_4 layer formed.

In the literature, a similar multilayer structure was observed for the P-type skutterudite $Ce_{0.9}Fe_3CoSb_{12}$ [42]. An interesting phenomenon called "pesting"-like oxidation explained the formation mechanism of multilayer structure on the material surface after 24-h exposure to air at 800 K. It was said that the severe oxide layers formed on the surface during the oxidation were periodically peeled off, leading to frequent oxidation of the fresh bulk material, which is still exposed to high concentration oxygen atmosphere. The reputation of oxidation & peeling off led to the formation of the multilayer structure. Clearly, the mechanisms for the formation of multilayer oxide structures depend highly on the materials (skutterudite in Ref. [42] vs half-Heusler in this study) and the oxidation testing methods (isothermal in Ref. [42] and cyclic in this study).

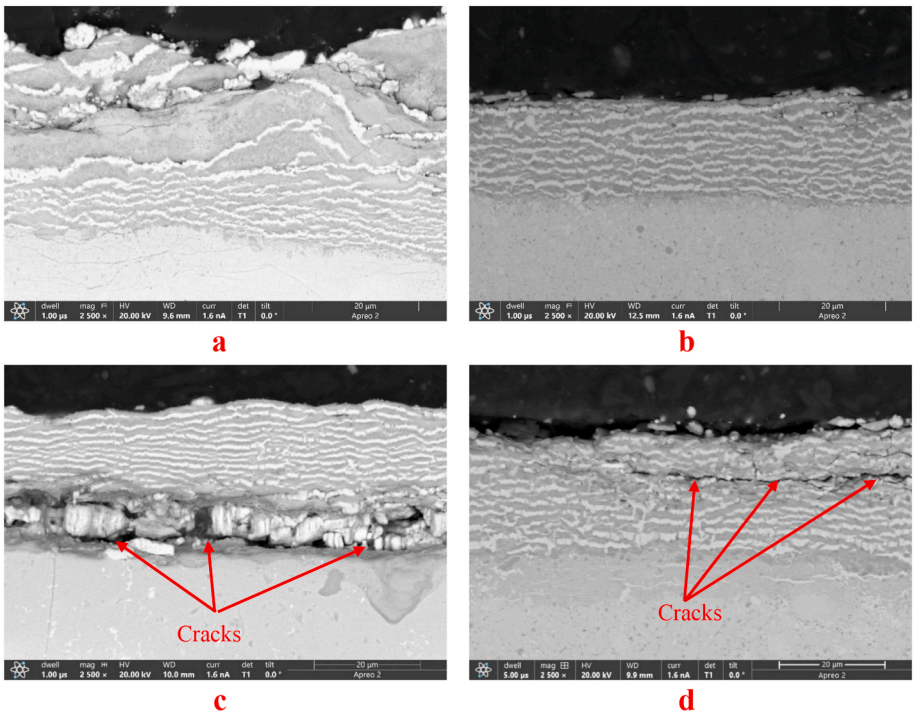

Fig. 5. Cross-sectional backscattering electron images of (a) N-10 sample, (b) P-10 sample, (c) N-50 sample, and (d) P-50 sample.

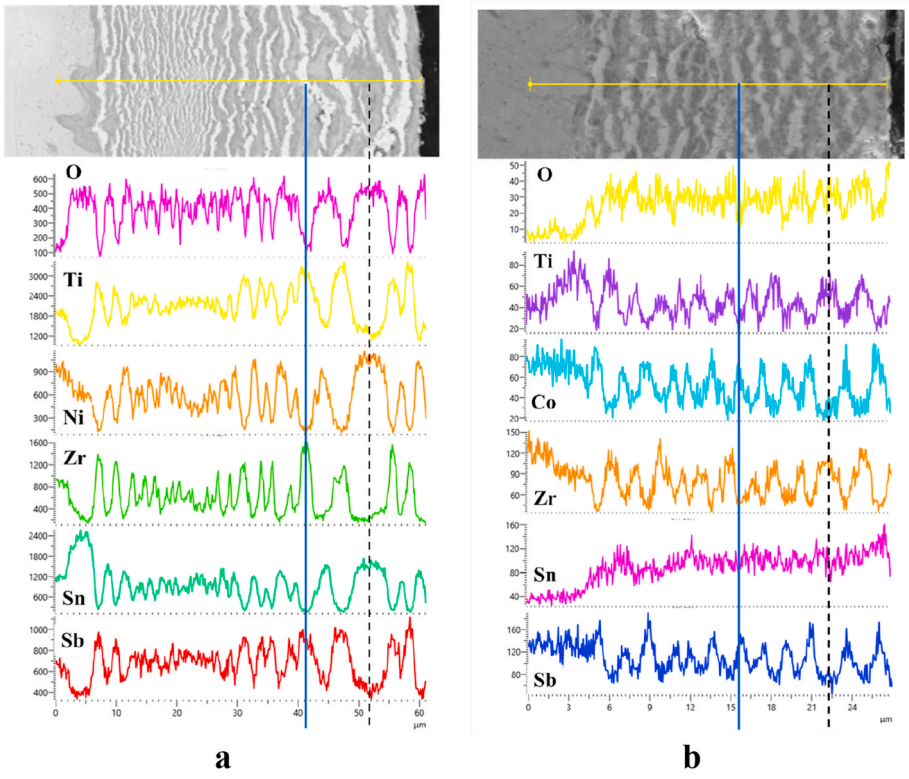

Fig. 6. EDS line scan analyses of (a) N-10, and (b) P-10 samples.

Due to the large difference in coefficient of thermal expansion (CTE) between ZrO_2 (~26.8×10^{-6} K^{-1}), SnO_2 (11.7×10^{-6} K^{-1}) and Ni_3Sn_4 (12.2×10^{-6} K^{-1}) [43–45], larger internal stress resulted in the formation of pinholes and cracks in the oxide layer as evidenced in Fig. 5c and schematically shown in Fig. 7d&e, which provided rapid paths for oxygen diffusion to the interface between the oxide layer and the matrix, and the process of forming $(Zr,Ti)O_2 + SnO_2 + Ni_3Sn_4$ layer structure is repeated thus resulting in the formation of oxides/Ni_3Sn_4 alternative layers.

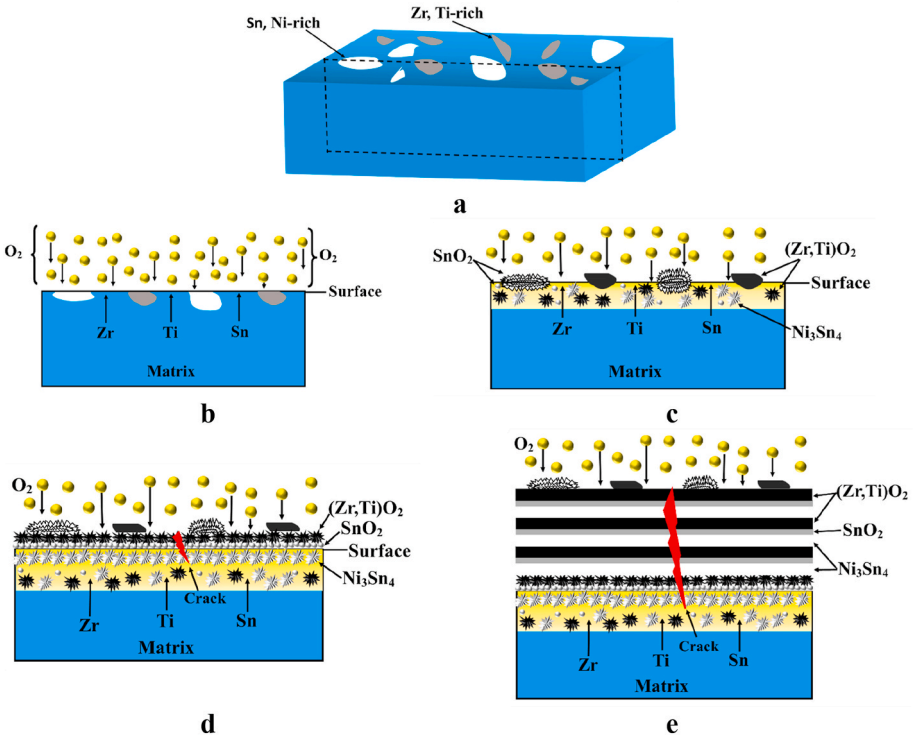

Fig. 7. Schematics of the formation of surface multilayered surface structure, (a) pre-oxidation of N-type sample, (b) inward diffusion of oxygen, (c) formation of SnO_2, $(Zr,Ti)O_2$ and Ni_3Sn_4 grains, (d) outward diffusion of Zr, Ti and Sn, starting the formation of $(Zr,Ti)O_2$, SnO_2 and Ni_3Sn_4 layers, (d) formation of multilayered surface structures.

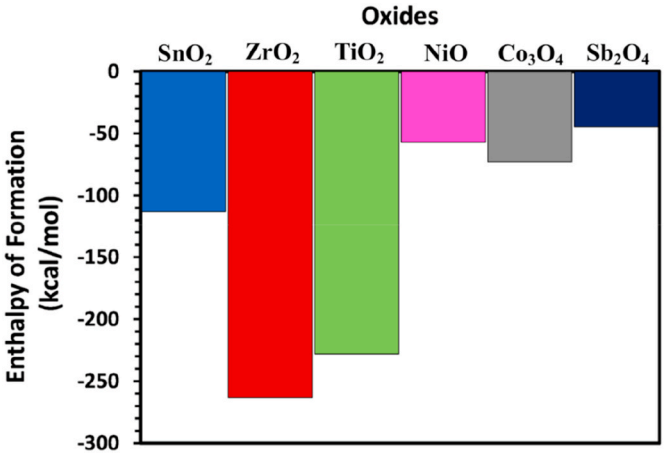

Fig. 8. Enthalpy of formation of potential oxide products.

4.2. Cyclic oxidation of P-type material

Although the alternating layer feature formed within the cross-sectional oxide case during cyclic oxidation on P-type (Zr,Ti)Co(Sn,Sb) (Fig. 5b&d) looks similar to that formed on the N-type (Zr,Ti)Ni(Sn,Sb) (Fig. 5a&c), the surface morphology (Fig. 4) and mass gain (Fig. 2) of the P-type (Zr,Ti)Co(Sn,Sb) are significantly different. Instead of the abnormal surface morphology change for the oxidised N-type samples, the P-type samples oxidised under the same conditions only showed small particles on a relatively smooth/flat surface (Fig. 4e&f) with very limited pinholes and mild cracks.

The mass gain of the P-type sample was 2.1 mg/cm^2 after 50 cycles, only one-third of the mass gain of the N-type samples when tested under the same cyclic oxidation conditions. It is also noticed that the mass mainly gained within the initial 20 cycles, and then it kept nearly constant when further increasing the oxidation cycles. The parabolic rate constants k_p calculated according to the parabolic kinetics, $(\Delta m/A)^2 = k_p \times t$, are 0.006165 mg^{2}cm^{-4}s^{-1} and 0.000109 mg^{2}cm^{-4}s^{-1} for N and P-type samples, respectively, with the former is more than 56.7 times that of the latter.

The smoother surface (Fig. 4e&f) and less mass gain (Fig. 2) indicate the better oxidation resistance of the P-type materials than the N-type ones, which is in line with the calculated much smaller parabolic rate constants. This significantly reduced parabolic rate constants and hence slackened oxidation process could be mainly attributed to the composition difference between the P-type and N-type materials. It can be seen from Table 1 that the P-type and N-type TE materials contain similar quantities of Zr and Ti elements, and similarly, $(Zr,Ti)O_2$ is formed in both N-type and T-type materials as identified by XRD analysis (Fig. 3).

Although both the N-type and P-type materials contain Sn, the P-type contains much less Sn (10.7 at.%) as compared with that (32.3 at.%) of the N-type. Firstly, the reduction of Sn in the P-type TE material could improve the oxidation resistance of the material. As can be seen from Fig. 4b&c, Sn initially segregated patches in the N-type material resulted in the formation of cauliflower-like tin oxides after 10 cycles and a large plateau with nano-crystalline tin oxides after 50 cycles of oxidation. The spallation of those features due to large difference in thermal expansion coefficient induced stress concentration increased the exposure surface areas to oxygen leading to fast oxidation. On the other hand, significantly reduced Sn content in the matrix should have helped to reduce the stress concentration, oxide spallation and hence oxidation of the P-type material.

Secondly, the Ni and reduced Sn in the P-type material are replaced by Co and Sb, respectively. The thermodynamic data shown in Fig. 8 also indicates that the enthalpy of formation ΔH of SnO_2 is more negative (−110 kcal/mol) than that for Co_3O_4 (−73 kcal/mol) and Sb_2O_4 (−45 kcal/mol). Therefore, the replaced Ni and Sn by Co and Sb, respectively, should have further contributed to the lower oxidation of the P-type

material [39,46]. It can be seen that the Sb content is significantly increased from <1.0 at. %) for the N-type material to 25.7 at. % in the P-type material. Accordingly, peaks of Sb_2O_4 are identified from the oxidation-tested P-type material. The enthalpy of formation ΔH of Sb_2O_4 is much less negative than all oxides as shown in Fig. 8 especially compared with that for ZrO_2 and TiO_2. Hence, this is reasonable to attribute the reduced oxidation rate of the P-type material as compared with the N-type material to the significantly high Sb content in the P-type material. Indeed, Sb_2O_4 has been used as a flame retardant in engineering plastics due to its stability in high temperature [47].

Thirdly, it is also reported that for the P-type TE material, the formation of Co_3O_4 oxide is exothermic [48], or entropy reduction reactions, the calculated ΔG changes from negative to positive with decreasing oxygen content [48], which was the case just beneath the firstly formed (Zr,Ti) oxides, such that the oxidation of Co was suppressed.

Having explained the slackened oxidation of the P-type TE material, the procedure for forming alternated layers in the surface oxide case on P-type material could be proposed as follows.

1) Inward diffused oxygen reacted with the (Zr,Ti)-rich patches formed small (Zr,Ti)O_2 particles, while those patches with high content of Sb and Sn reacted with oxygen formed a few Sb_2O_4 and SnO_2 particles, see Fig. 4.
2) The remaining procedures would be similar to that for the formation of the alternated layer in N-type by replacing the Ni with Co, reducing Sn and increasing Sb, such that the alternated layers are (Zr,Ti)O_2 + SnO_2 (very thin) + Sb_2O_4 + CoSb.

5. Conclusions

In this study, the oxidation behaviour of the Hf-free N-type (Zr,Ti)Ni(Sn,Sb) and P-type (Zr,Ti)Co(Sn,Sb) thermoelectric materials produced by mechanical alloying and sintering at 800 °C were investigated by cyclic oxidation between room temperature and 500 °C for up to 50 cycles. Based on the experimental findings, the following conclusions can be drawn.

- The surfaces of both N-type (Zr,Ti)Ni(Sn,Sb) and P-type (Zr,Ti)Co(Sn,Sb) materials are entirely oxidised after the cyclic oxidation testing, leading to a significant change in the surface morphologies.
- The oxidation of both N-type and P-type materials under cyclic oxidation conditions follows parabolic oxidation kinetics. However, the mass gain of the N-type increased much faster compared to that of the P-type with the parabolic rate constants being 0.006165 $mg^2cm^{-4}s^{-1}$ and 0.000109 $mg^2cm^{-4}s^{-1}$ for N and P-type materials, separately.
- An alternated multilayer structure was formed on the cross-sections of both N-type and P-type materials, which highly suffered from aggressive oxidation. It is believed that such severe oxidation-induced microstructural changes would negatively affect the thermoelectric performance of these materials, which are constantly subjected to temperature differential.

The findings from the present study suggest in order to improve the thermal stability of N-type and P-type half-Heusler materials with favourable thermoelectric performance, it is necessary to protect the TE materials against oxidation by developing advanced surface coatings such as the CrSi coating developed recently in our group. Very promising oxidation protection results are obtained, which will be published in another paper.

Declaration of competing interest

The authors declare that they have no known competing financial interests or personal relationships that could have appeared to influence the work reported in this paper.

Acknowledgement

The authors appreciate MATRES Scrl (Italy) for supplying the synthesized and consolidated TE blocks. This research was funded by the EU H2020 Project 'FAST and Nano-enabled SMART materials, Structure and System for Energy Harvesting' (FAST-SMART) under Grant no. 862289. One of the authors (M.G.) thanks for the PhD studentship provided by the Ministry of National Education of the Republic of Türkiye.

References

[1] Chen G, et al. Recent developments in thermoelectric materials. Int Mater Rev 2003;48(1):45–66.
[2] Mukherjee M, Srivastava A, Singh AK. Recent advances in designing thermoelectric materials. J Mater Chem C 2022;10(35):12524–55.
[3] Ma Z, et al. Review of experimental approaches for improving zT of thermoelectric materials. Mater Sci Semicond Process 2021;121:105303.
[4] Wei J, et al. Review of current high-ZT thermoelectric materials. J Mater Sci 2020;55:12642–704.
[5] Jiang B, et al. High figure-of-merit and power generation in high-entropy GeTe-based thermoelectrics. Science 2022;377(6602):208–13.
[6] Meroz O, Elkabets N, Gelbstein Y. Enhanced thermoelectric properties of N-type Bi2Te3–x Se x alloys following melt-spinning. ACS Appl Energy Mater 2019;3(3):2090–5.
[7] Liu H-T, et al. High-performance in N-type PbTe-based thermoelectric materials achieved by synergistically dynamic doping and energy filtering. Nano Energy 2022;91:106706.
[8] Komisarchik G, Gelbstein Y, Fuks D. Solubility of Ti in thermoelectric PbTe compound. Intermetallics 2017;89:16–21.
[9] Kaller M, Fuks D, Gelbstein Y. Sc solubility in P-type half-Heusler (Ti1-cScc) NiSn thermoelectric alloys. J Alloys Compd 2017;729:446–52.
[10] Bano S, et al. Room temperature Bi2Te3-based thermoelectric materials with high performance. J Mater Sci Mater Electron 2020;31(11):8607–17.
[11] Cao T, et al. Advances in bismuth-telluride-based thermoelectric devices: progress and challenges. eScience 2023:100122.
[12] Witting IT, et al. The thermoelectric properties of bismuth telluride. Advanced Electronic Materials 2019;5(6):1800904.
[13] Shtern Y, et al. Challenges and perspective recent trends of enhancing the efficiency of thermoelectric materials on the basis of PbTe. Mater Today Commun 2023:107083.
[14] Zhou Y. Progress and trend of PbTe based thermoelectric materials. In: Journal of Physics: conference series. IOP Publishing; 2022.
[15] Hao X, et al. Performance optimization for PbTe-based thermoelectric materials. Front Energy Res 2021;9:754532.
[16] Chauhan NS, et al. Enhanced thermoelectric performance in Hf-Free P-type (Ti, Zr) CoSb half-heusler alloys. J Electron Mater 2019;48:6700–9.
[17] Van Du N, et al. Enhanced thermoelectric properties of Hf-free half-Heusler compounds prepared via highly fast process. J Alloys Compd 2021;886:161293.
[18] Liu Z, et al. Design of high-performance disordered half-Heusler thermoelectric materials using 18-electron rule. Adv Funct Mater 2019;29(44):1905044.
[19] Sun Q, et al. Structural evolution of high-performance Mn-alloyed thermoelectric materials: a case study of SnTe. Small 2021;17(25):2100525.
[20] Tian B-Z, et al. Enhanced thermoelectric performance of SnTe-based materials via interface engineering. ACS Appl Mater Interfaces 2021;13(42):50057–64.
[21] Moshwan R, et al. Eco-friendly SnTe thermoelectric materials: progress and future challenges. Adv Funct Mater 2017;27(43):1703278.
[22] Cheng X, Farahi N, Kleinke H. Mg 2 Si-based materials for the thermoelectric energy conversion. Jom 2016;68:2680–7.
[23] Zhou Z, et al. High-performance magnesium-based thermoelectric materials: progress and challenges. J Magnesium Alloys 2022;10(7):1719–36.
[24] Nieroda P, et al. The structural, microstructural and thermoelectric properties of Mg2Si synthesized by SPS method under excess Mg content conditions. J Alloys Compd 2019;775:138–49.
[25] Ioannou IA. P-type half-Heusler and Bismuth-Telluride thermoelectric materials. 2022.
[26] Ioannou I, et al. Reduction of Hf via Hf/Zr substitution in mechanically alloyed (Hf, Ti) CoSb half-heusler solid solutions. INORGA 2022;10(4):51.
[27] Zhang X, et al. Ultralow lattice thermal conductivity and improved thermoelectric performance in a Hf-free half-Heusler compound modulated by entropy engineering. J Mater Chem A 2023;11(15):8150–61.
[28] Chauhan NS, et al. Compositional tailoring for realizing high thermoelectric performance in hafnium-free N-type ZrNiSn half-heusler alloys. ACS Appl Mater Interfaces 2019;11(51):47830–6.
[29] Zhang Q, et al. Enhanced thermoelectric performance of Hafnium free N-type ZrNiSn half-Heusler alloys by isoelectronic Si substitution. Materials Today Physics 2022;24:100648.
[30] Min R, et al. Significantly improved thermoelectric properties of Nb-doped ZrNiSn half-Heusler compounds. Chem Eng J 2022;449:137898.
[31] Barako MT, et al. Thermal cycling, mechanical degradation, and the effective figure of merit of a thermoelectric module. J Electron Mater 2013;42(3):372–81.

[32] Kang HB, et al. Understanding oxidation resistance of half-Heusler alloys for in-air high temperature sustainable thermoelectric generators. ACS Appl Mater Interfaces 2020;12(32):36706–14.
[33] Yamini SA, et al. Fabrication of thermoelectric materials–thermal stability and repeatability of achieved efficiencies. J Mater Chem C 2015;3(40):10610–5.
[34] Skomedal G, et al. Methods for enhancing the thermal durability of high-temperature thermoelectric materials. J Electron Mater 2014;43:1946–51.
[35] Sootsman JR, Chung DY, Kanatzidis MG. New and old concepts in thermoelectric materials. Angew Chem Int Ed 2009;48(46):8616–39.
[36] Zheng Y, et al. Defect engineering in thermoelectric materials: what have we learned? Chem Soc Rev 2021;50(16):9022–54.
[37] Kikuchi D, Tadokoro J, Eguchi T. The high-temperature thermoelectric properties of polycrystalline Ba 8 Ga x Al y Si 46− x− y type-I clathrates. J Electron Mater 2014;43:2141–4.
[38] Weast RC. Handbook of chemistry and physics. 1st Student Edition. Boca Raton, Florida: CRC-Press; 1988. p. 69.
[39] Wang L, et al. High temperature oxidation behavior of ZrNiSn-based half-Heusler thermoelectric material. Corrosion Sci 2023;225:111606.
[40] Appel O, et al. Surface oxidation of TiNiSn (Half-Heusler) alloy by oxygen and water vapor. Materials 2018;11(11):2296.
[41] Berche A, Jund P. Oxidation of half-Heusler NiTiSn materials: implications for thermoelectric applications. Intermetallics 2018;92:62–71.
[42] Qiu P, et al. "Pesting"-like oxidation phenomenon of P-type filled skutterudite Ce0. 9Fe3CoSb12. J Alloys Compd 2014;612:365–71.
[43] Patil R, Subbarao E. Axial thermal expansion of ZrO2 and HfO2 in the range room temperature to 1400° C. J Appl Crystallogr 1969;2(6):281–8.
[44] Spencer JA, et al. A review of band structure and material properties of transparent conducting and semiconducting oxides: Ga2O3, Al2O3, In2O3, ZnO, SnO2, CdO, NiO, CuO, and Sc2O3. Appl Phys Rev 2022;9(1).
[45] Ohno H, Kanzawa Y. Internal oxidation in gold alloys containing small amounts of Fe and Sn. J Mater Sci 1983;18:919–29.
[46] Wiberg E, Wiberg N. Inorganic chemistry. Academic press; 2001.
[47] Alwash NA, et al. Fire retardancy characteristics of polymeric composite materials. Baghdad Science Journal 2013;10 (3عدد خاص بمؤتمر الكيمياء).
[48] Gu J, et al. High-temperature oxidation mechanism of ZrCoSb-based half-Heusler thermoelectric compounds. J Mater Sci Technol 2023;148:242–9.